FOSSEE, IIT Bombay
OpenFOAM Research Migration Project
May 2025

Numerical Simulation of a Fixed-Wing UAV and the Effect of Blended Winglets

Toran Bahadur Niroula[1], Nikhil Bhamare[2], Tushar Chourushi[3], and Chandan Bose[4]

[1]Undergraduate student, Department of Mechanical and Aerospace Engineering, Pulchowk Campus
[2]CFD Engineer, CFD Baba
[3]Assistant Professor, Department of Aerospace Engineering, MIT Art, Design and Technology University, Pune, Maharashtra 412201, India
[4]Assistant Professor, Aerospace Engineering, College of Engineering and Physical Sciences, The University of Birmingham

May 30, 2025

Synopsis

This research migration study aims to replicate and extend the work "Numerical Simulation of a Flow Around an Unmanned Aerial Vehicle" by S.M.A. Meftah et al. using the open-source computational fluid dynamics (CFD) software OpenFOAM. The study investigates the aerodynamic performance of a small fixed-wing unmanned aerial vehicle (UAV) with an inverted V-tail, a configuration relevant for various civil and defence applications such as aerial surveillance and reconnaissance, environmental and disaster monitoring, and remote delivery. This makes it necessary to accurately model flow separation and tail-wing interactions, as well as assess the effect of geometric modifications like winglets while using validated and computationally affordable models. This study employs `simpleFoam`, a steady-state incompressible solver in OpenFOAM, and uses the Spalart–Allmaras (SA) turbulence model, which aligns with the reference study. The half-domain model is used, taking advantage of the longitudinal symmetry found in cruise to reduce computational cost. An unstructured mesh is generated using `snappyHexMesh`, with refinement and local surface feature resolution near the surface of the UAV. Mesh independence is verified using the lift coefficient, and results are validated against the experimentally validated numerical results of Meftah et al. Furthermore, the study examines the effect of blended winglets with cant angles of 90° and 45° at a constant sweep and taper ratio, revealing a maximum lift-to-drag ratio improvement of 14.95% at a 45° cant angle compared to the baseline design. These results confirm that the exploration of the winglet design can enhance aerodynamic performance without altering the geometry of the main wing. The work provides insight into effective design strategies for performance enhancement in small-scale UAVs, helping bridge the gap between academic CFD studies and practical UAV development.

Keywords: OpenFOAM, simpleFoam, UAV, RANS, turbulence modelling, winglets

1 Introduction

Unmanned Aerial Vehicles (UAVs) have become indispensable tools across civilian and military domains, enabling missions such as remote sensing, surveillance, environmental monitoring, and package delivery. Their low cost, operational flexibility, and capability to reach inaccessible areas have made them a dominant research and development frontier in the aerospace sector [1]. In particular, fixed-wing UAVs with inverted V-tail configurations offer structural and aerodynamic advantages that are relevant to long-endurance and medium-range applications. A key performance metric for such UAVs is aerodynamic efficiency, typically expressed as the lift-to-drag (L/D) ratio. Enhancing L/D improves flight endurance and energy efficiency, which are crucial for both battery-powered systems (EPUAV) and missions with tight payload constraints. Among various techniques for aerodynamic enhancement, winglets have demonstrated notable benefits in reducing induced drag by mitigating wingtip vortices [2]. While extensively studied in commercial aircraft, their design optimisation for small-sized UAVs remains a topic of growing interest, especially as these platforms operate in low Reynolds number and low Mach number regimes where laminar-turbulent transition and flow separation become significant. Previous work by Meftah et al. [3] numerically analysed the flow over a small-scale UAV in ANSYS Fluent using the Spalart–Allmaras turbulence model, with validation based on experimental results for an isolated wing. However, their study did not explore the influence of winglets or alternate design configurations on aerodynamic performance. The present study intends to migrate and extend the work from Meftah et al. by replicating their baseline configuration using OpenFOAM and extending the analysis to assess the aerodynamic influence of blended winglets with varying cant angles (45° and 90°). The simulations are performed at multiple angles of attack under incompressible flow conditions at a freestream velocity of 20 m/s. The Spalart–Allmaras turbulence model is employed throughout the study. Mesh generation is performed using `snappyHexMesh`, employing unstructured grids with surface and wake refinement. Grid convergence is verified by monitoring aerodynamic coefficients.

To emphasise the practical implications of this work, we note that the configuration studied bears a strong resemblance to real-world UAVs such as the Albatross UAV by Applied Aeronautics, the Mugin 3200 V-tail UAV platform by MuginUAV, which feature a similar wingspan and inverted V-tail structure. Although the present model is generic and does not mimic a specific commercial design, the aerodynamic insights are broadly applicable to UAVs in this class.

Source: botsanddrones.co

(a) Albatross by Applied Aeronautics

Source: muginuav.com

(b) Mugin 3200 by MuginUAV

2 Governing Equations

The fluid flow in this study is modelled using the Reynolds-Averaged Navier-Stokes (RANS) equations [4]. These equations describe the conservation of mass and momentum for a viscous fluid. The simulations are performed under the assumptions of steady-state, incompressible external flow. External body forces are considered negligible. The turbulence effects are accounted for by employing the Spalart-Allmaras one-equation turbulence model [5].

2.1 Reynolds-Averaged Navier-Stokes Equations

For steady-state, incompressible turbulent flow, the time-averaged continuity and momentum equations are expressed as follows [4]:

The continuity equation ensures the conservation of mass and is given by:

$$\nabla \cdot \mathbf{u} = 0 \tag{1}$$

where $\mathbf{u}$ is the mean velocity vector.

The momentum equation describes the conservation of momentum:

$$\rho(\mathbf{u} \cdot \nabla)\mathbf{u} = -\nabla p + \nabla \cdot \left[(\mu + \mu_t)\left(\nabla \mathbf{u} + (\nabla \mathbf{u})^T\right)\right] \tag{2}$$

Here,

- ρ is the fluid density.
- p is the mean pressure.
- μ is the dynamic viscosity of the fluid.
- μ_t represents the turbulent eddy viscosity determined by the Spalart-Allmaras turbulence model.
- $(\nabla \mathbf{u} + (\nabla \mathbf{u})^T)$ is the mean strain rate tensor.

2.2 Spalart-Allmaras Turbulence Model

The Spalart-Allmaras (SA) model is a one-equation turbulence model that solves a transport equation for a modified turbulent kinematic viscosity, denoted as $\tilde{\nu}$ [5]. The governing transport equation for $\tilde{\nu}$ is:

$$\mathbf{u} \cdot \nabla \tilde{\nu} = c_{b1}\tilde{S}\tilde{\nu} - c_{w1} f_w \left(\frac{\tilde{\nu}}{d}\right)^2 + \frac{1}{\sigma}\left[\nabla \cdot ((\nu + \tilde{\nu})\nabla \tilde{\nu}) + c_{b2}(\nabla \tilde{\nu})^2\right] \tag{3}$$

where:

- $\tilde{\nu}$ is the modified turbulent kinematic viscosity.
- ν is the molecular kinematic viscosity ($\nu = \mu/\rho$).

- d is the distance to the nearest wall.
- $\tilde{S}$ is a modified vorticity magnitude.
- f_w is a wall damping function.
- $c_{b1}, c_{b2}, c_{w1}, \sigma$ are model constants.

The turbulent kinematic viscosity ν_t is computed from $\tilde{\nu}$ using the relation:

$$\nu_t = \tilde{\nu} f_{v1} \tag{4}$$

where f_{v1} is a viscous damping function defined as:

$$f_{v1} = \frac{\chi^3}{\chi^3 + c_{v1}^3}, \quad \text{with} \quad \chi = \frac{\tilde{\nu}}{\nu} \tag{5}$$

and c_{v1} is another model constant. The turbulent dynamic viscosity μ_t, used in the RANS momentum equation (2), is then calculated as:

$$\mu_t = \rho \nu_t \tag{6}$$

The modified vorticity magnitude $\tilde{S}$ and the wall damping function f_w are given by:

$$\tilde{S} = \Omega + \frac{\tilde{\nu}}{\kappa^2 d^2} f_{v2} \tag{7}$$

$$f_w = g \left(\frac{1 + c_{w3}^6}{g^6 + c_{w3}^6} \right)^{1/6}, \quad \text{with} \quad g = r + c_{w2}(r^6 - r) \tag{8}$$

where Ω is the magnitude of the mean vorticity vector ($\Omega = |\nabla \times \mathbf{u}|$), κ is the von Kármán constant, and f_{v2} is another damping function, typically defined as $f_{v2} = 1 - \frac{\chi}{1+\chi f_{v1}}$. The variable r is defined as:

$$r = \min \left(\frac{\tilde{\nu}}{\tilde{S} \kappa^2 d^2}, 10 \right) \tag{9}$$

The standard model constants commonly used are:
$c_{b1} = 0.1355$, $c_{b2} = 0.622$, $\sigma = 2/3$, $\kappa = 0.41$, $c_{w1} = c_{b1}/\kappa^2 + (1 + c_{b2})/\sigma$, $c_{w2} = 0.3$, $c_{w3} = 2$, $c_{v1} = 7.1$ [5].
The Spalart-Allmaras model is widely employed for aerodynamic flow simulations due to its computational efficiency and robustness, particularly in predicting attached boundary layers and mildly separated flows.

3 Computational Methodology

Generally, small-sized UAVs operate at Reynolds numbers ranging from 10^5 to 10^6 [6]. Meftah et al. analysed their UAV design at a speed of 20 m/s [3]. The corresponding Reynolds number for the UAV operating at 20 m/s and the standard atmosphere at sea level with kinematic viscosity of 1.5×10^{-5} with the characteristic length of 0.236 m is 0.315×10^6. For UAV and external flow in low Reynolds number At low subsonic speed, the following key assumptions can be made:

1. Incompressible flow
2. Steady flow
3. Turbulent flow
4. Isothermal flow
5. No external force
6. Rigid UAV surface

Using these assumptions, a simplified model of the UAV can be realised, and the flow around it can be numerically solved.

3.1 Geometry and Computational Domain

The geometry of the UAV was replicated as much as possible based on the information available from Meftah et al. The longitudinal half geometry of the UAV was created in CATIA V5R21, assuming symmetry about the plane created by longitudinal and vertical axes. As the UAV is simulated for steady-state flight conditions, there is essentially no side slip angle. So, the symmetry condition is justified. The geometry created in CATIA was exported as an STL file. Cleaning the STL file was performed using meshLab, correcting any discrepancies in geometry.

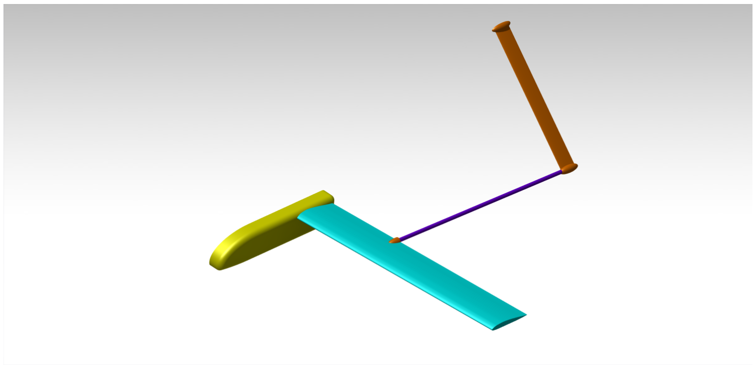

Figure 2: Isometric view of the UAV geometry

The UAV features an inverted V-tail configuration and a twin boom. It has a projected wingspan of 2900 mm, a total length of 1955 mm, a wing chord of 236 mm, and a projected tail span of 1080 mm, center-to-center distance between nose and main landing gear wheels of 754 mm, dihedral angle of 4° and wing incidence of 4° [3]. Other specific dimensions like total length, breadth, and height of fuselage, distance between wing leading edge and tail leading edge, and the chord length of the tail were not available, so they were appropriately estimated based on the proportion in the figures. The UAV has **Clark YH** airfoil on wings and **NACA 0012** airfoil on tail.

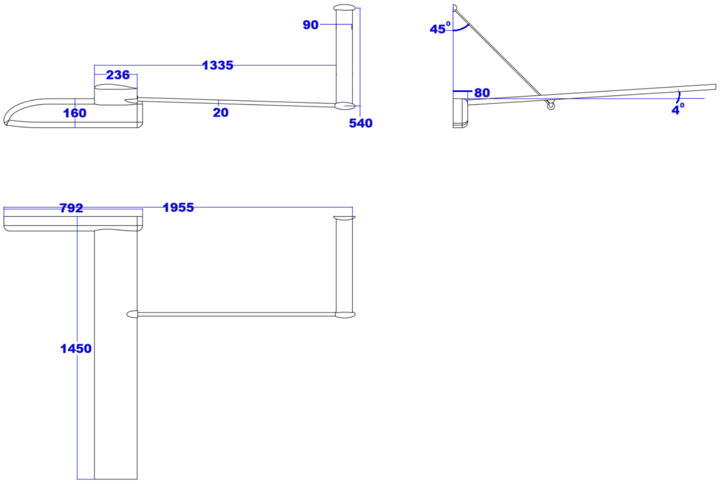

Figure 3: 3D view of the UAV configuration

The missing geometry information was assumed appropriately, like fuselage length of 792 mm, fuselage height and width of 160 mm, tail chord of 90 mm, wing leading edge to tail leading edge distance of 1335 mm, tail boom diameter of 20mm, etc.

The domain size is generally taken to be about 15 to 20 times the largest dimension along the length, and 5 to 10 times the highest dimension along the width for width and height. Based on this, the domain size of 30 m length, 15 m height and 7.5 m half-width was chosen.

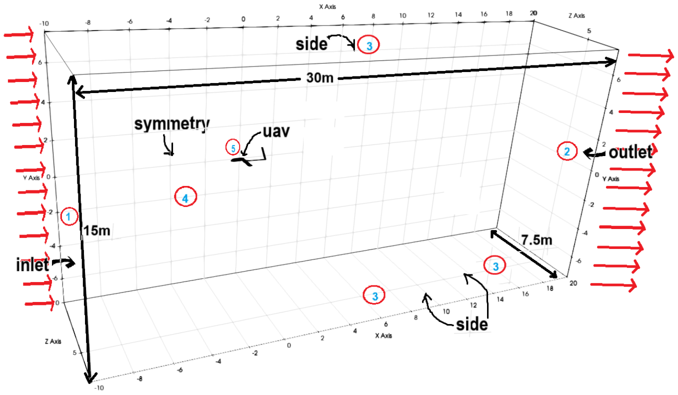

Figure 4: Simulation domain setup for the UAV CFD analysis

The effect of a blended winglet at two different cant angles was studied using wingtip devices. The baseline geometry in CATIA was modified to add a winglet of about a similar surface area, having an equal taper ratio. An extension of around 0.05 m was made on the wing, and a winglet of 0.2 m was blended to create a smoother geometry transition. The projected area of baseline UAV, UAV with winglet at 90° and UAV with winglet at 45° are 0.3422 m^2, 0.3732 m^2, and 0.3889 m^2, respectively. The winlets are unswept at the leading edge and have a tip chord of 0.1 m.

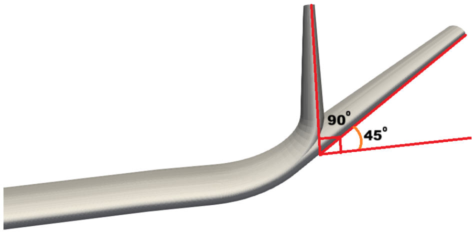

Figure 5: Winglet geometry

3.2 Mesh Generation

Mesh generation was performed using `blockMesh` and `snappyHexMesh` utilities, which are included in the openFoam toolbox. `blockMesh` was used to generate the rectangular domain. To improve the accuracy of the simulation without inflating computational cost, edge grading was done to get smaller cells in the region near the surface of the UAV and larger cells near the boundary of the domain, except for the symmetry region. `snappyHexMesh` was used to generate an unstructured 3D mesh from the STL file generated by CATIA. The surface refinement was performed on the surface of the UAV, whereas refinement was performed with a box enclosing the UAV and the wake region. Layers were added for boundary layer resolution.

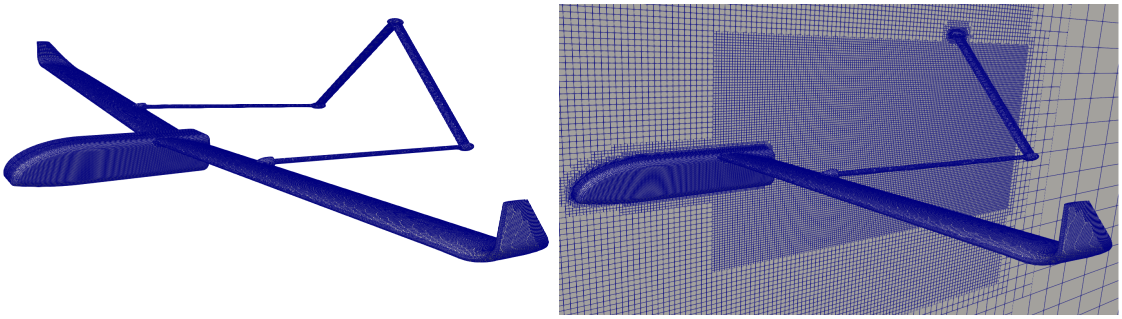

Figure 6: Mesh structure of the UAV surface

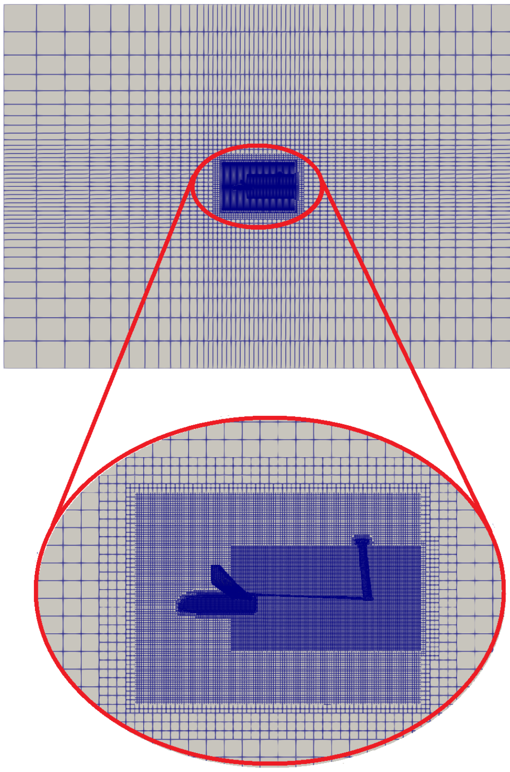

Figure 7: Detailed mesh visualisation of the UAV

3.3 Solver Setup

Based on the simplified model of fluid domain and computational constraints, a RANS solver for steady, incompressible, isothermal flow is required. The numerical simulation of the steady, incompressible external flow was performed using the SimpleFoam solver within the OpenFOAM v2406 framework. SimpleFoam is a widely used solver for steady-state incompressible flow, employing a finite volume discretisation of the governing Navier-Stokes equations. The Semi-Implicit Method for Pressure-Linked Equations (SIMPLE) algorithm is used to handle the pressure-velocity coupling. This algorithm iteratively solves the momentum equation to obtain a velocity field, corrects the pressure field using a pressure equation derived from the continuity equation, and then corrects the velocity field. This process repeats until convergence is achieved. The Spalart-Allmaras (SA) Reynolds Averaged Navier Stokes (RANS) turbulence model was selected to model the turbulent flow. The SA model is a one-equation model that solves a transport equation for a modified turbulent viscosity. It is known for its robustness and relatively low computational cost, making it suitable for external aerodynamic flows, especially for wall-bounded flows, where accurate prediction of the boundary layer is important. Convergence of the solution was monitored using the `residualControl` feature in the `fvSolution` dictionary. The convergence criteria for the key variables are summarised in Table 1.

Table 1: Convergence Criteria

Variable	Tolerance
Pressure (p)	1×10^{-5}
Velocity (U)	1×10^{-6}
Turbulent Kinetic Energy (k)	1×10^{-6}
Specific Dissipation Rate (omega)	1×10^{-6}
Modified Turbulent Viscosity (nuTilda)	1×10^{-6}

These tolerance values represent the maximum allowable residual for each variable, ensuring that the solution reaches an acceptable level of accuracy. The relative tolerance (`relTol`) was also specified for each variable to control the relative reduction of the residual at each iteration. The linear systems of equations resulting from the discretisation of the governing equations were solved using the methods summarised in Table 2. Under-relaxation factors, also shown in Table 2, were used to improve the stability of the iterative solution process.

Table 2: Equation Solvers and Under-Relaxation Factors

Variable	Solver	smoother	Under-Relaxation Factor
Pressure (p)	GAMG	Gauss-Seidel	0.3
Velocity (U)	smoothSolver	Gauss-Seidel	0.7
Turbulent Kinetic Energy (k)	smoothSolver	Gauss-Seidel	0.5
Specific Dissipation Rate (omega)	smoothSolver	Gauss-Seidel	0.5
Modified Turbulent Viscosity (nuTilda)	smoothSolver	Gauss-Seidel	0.7

The Geometric-Algebraic Multi-Grid (GAMG) solver was used for the pressure equation, while the `smoothSolver` was used for the momentum and turbulence equations. The discretisation schemes employed for various terms in the governing equations are detailed in Table 3.

Table 3: Discretization Schemes

Term	Scheme
Time Derivative	Steady State
Gradient	Gauss Linear (with cell limiting for U, nuTilda)
Divergence	Gauss Linear Upwind (for velocity) Bounded Gauss Limited Linear (for turbulence) Gauss Linear (for viscous term)
Laplacian	Gauss Linear Corrected
Interpolation	Linear

Boundary and Initial Conditions

The boundary conditions for the velocity ($\mathbf{U}$), pressure (p), turbulent kinematic viscosity (ν_t), and $\tilde{\nu}$ fields are summarized in Table 4. The initial conditions are uniform throughout the domain.

Table 4: Boundary Conditions

Boundary	$\mathbf{U}$	p	$\tilde{\nu}$
Inlet	$(20\cos(\alpha), 20\sin(\alpha), 0)$	`zeroGradient`	uniform 1×10^{-5}
Outlet	`inletOutlet`	uniform 0	`zeroGradient`
UAV	`noSlip`	`zeroGradient`	uniform 0
Side	`freestream`	`zeroGradient`	`freestream`
Symmetry	`symmetryPlane`	`symmetryPlane`	`symmetryPlane`

The initial conditions for all fields were set to uniform values of $p = 0$, $\nu_t = 0$, and $\tilde{\nu} = 1 \times 10^{-5}$.

3.4 Post-processing and Data Extraction

After parallel execution of the CFD simulations, a comprehensive post-processing procedure was used to extract and visualise the relevant flow field data. ParaView, an open-source multi-platform data analysis and visualisation application, was the primary tool for visualising the simulation results. ParaView's capabilities were utilised to generate contour plots and vector field representations, providing detailed insights into the flow patterns around the UAV. Pressure contours and velocity magnitude were visualised on the UAV's surface and the flow field's cross-section.

To quantitatively assess the aerodynamic performance of the UAV, the lift and drag coefficients were computed directly during the simulation runtime using the 'forceCoeffs' function object, utilising the 'forces' library. This function object integrates pressure and viscous forces over the specified surface patches. It calculates the non-dimensional coefficients based on user-defined parameters, namely density, magnitude of velocity, direction of forces, and reference area. The lift coefficient (C_L) and drag coefficient (C_D) computed by this function object are [7]:

$$C_L = \frac{L}{\frac{1}{2}\rho_\infty U_\infty^2 S_{ref}} \tag{10}$$

$$C_D = \frac{D}{\frac{1}{2}\rho_\infty U_\infty^2 S_{ref}} \tag{11}$$

where L and D are the integrated force components in the specified forces directions, ρ_∞ is the density of air, U_∞ is the magnitude of velocity of UAV, and S_{ref} is the area of wings projected on horizontal plane. The angle of attack is the angle made by the velocity vector with a chord of the wing in the vertical plane. For subsequent analysis and plotting, these coefficient data were extracted and processed using Python scripts. The Matplotlib library, alongside the NumPy library, was employed to generate plots of the aerodynamic coefficients versus angle of attack.

4 Results and Discussions

4.1 Turbulence Model Validation

To ensure solution robustness, the K Omega SST and Spalart-Allmaras (SA) turbulence models were compared. Both models agreed well in the linear range. However, SA predicted a more gradual stall compared to the K Omega SST model. This small discrepancy arises because the two-equation K Omega SST model resolves turbulent length scales more effectively than the one-equation SA model. The Spalart-Allmaras (SA) model is more forgiving in terms of mesh quality and convergence compared to the K Omega SST model.

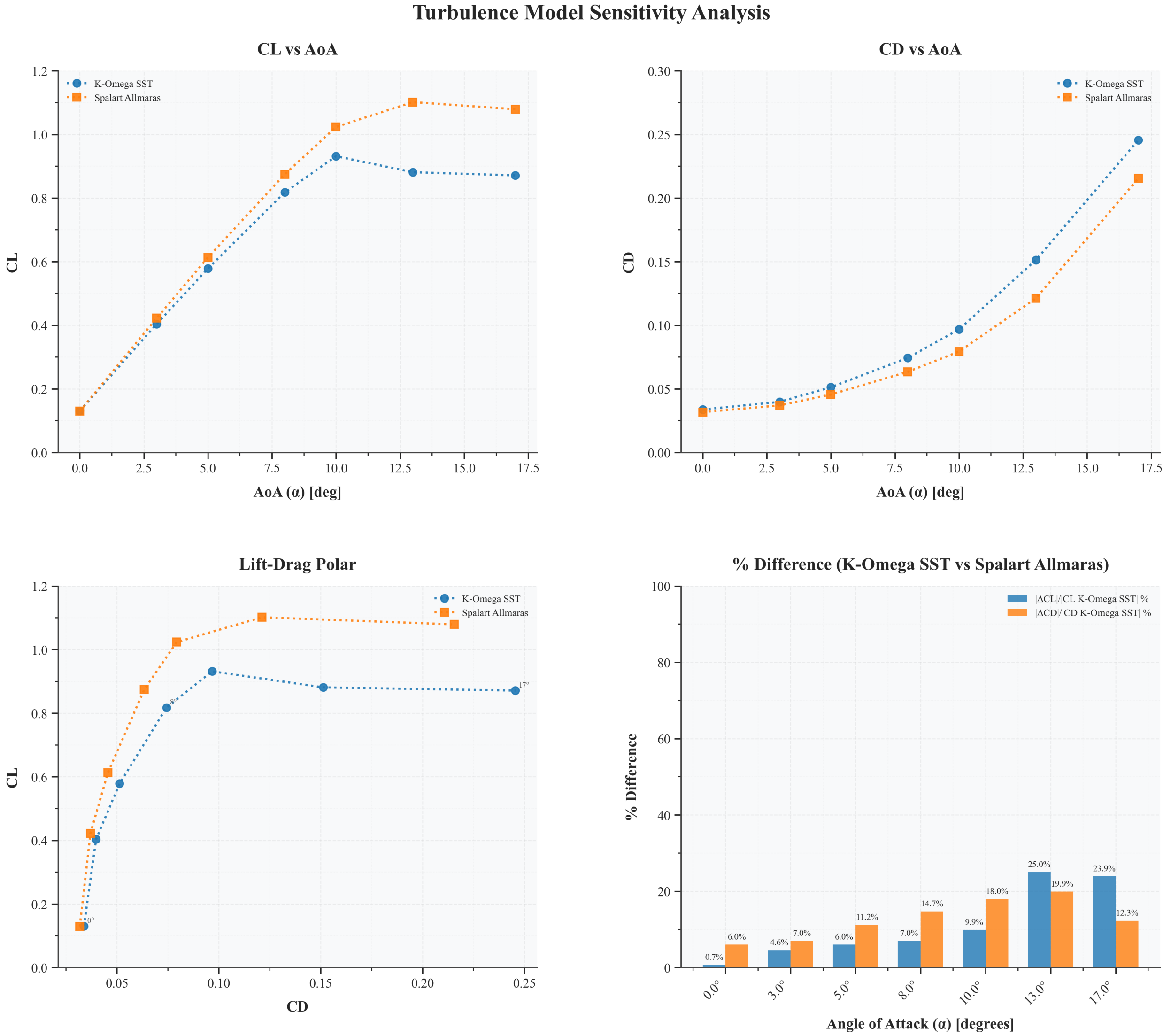

Figure 8: Comparison of aerodynamic performance prediction between K-Omega SST and Spalart-Allmaras turbulence models.

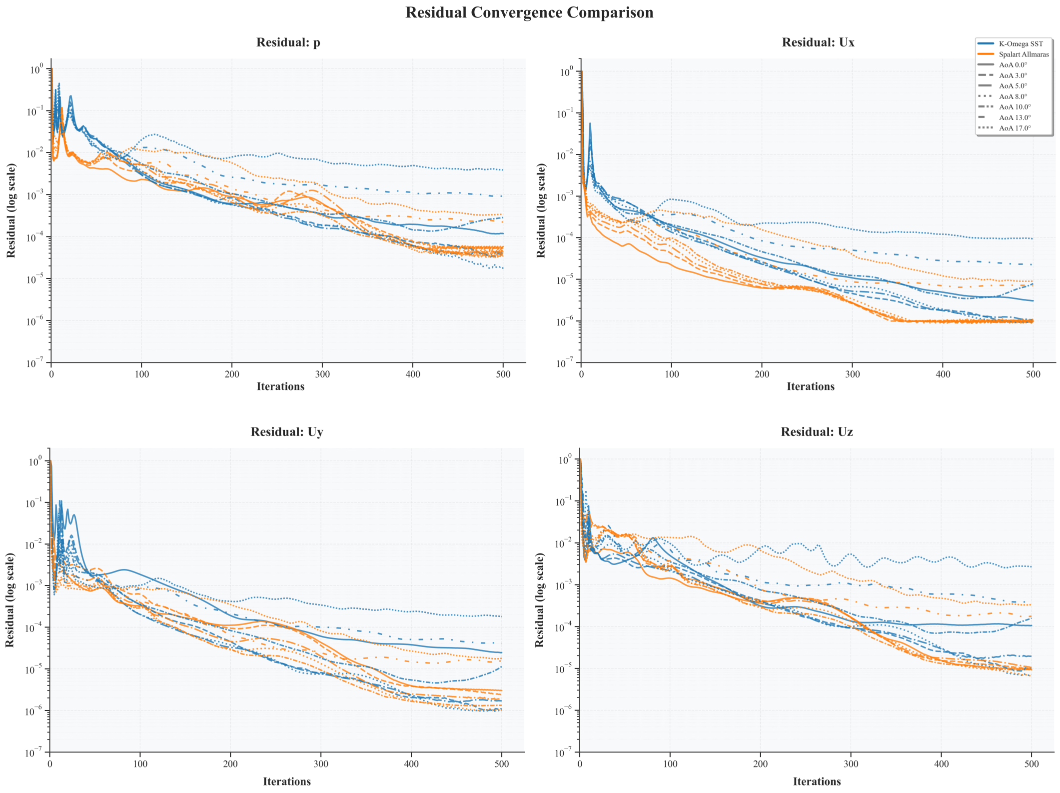

Figure 9: Comparison of residual convergence between K-Omega SST and Spalart-Allmaras turbulence models.

Although the K-Omega SST model is generally favoured for accurately resolving flow separation, the Spalart-Allmaras (SA) model was chosen for this study as it balances computational efficiency and accuracy well. The SA model provides a computationally efficient solution given the study's focus on overall aerodynamic performance.

4.2 Grid Convergence Study

A grid convergence study was performed to ensure the numerical solution is independent of the mesh resolution. Simulations were carried out for the baseline UAV configuration at an angle of attack of 4°, using three different mesh densities as summarised in Table 5.

Table 5: Mesh configurations used for the grid convergence study

Grid Level	**Cell Count (Millions)**
Coarse	1.04
Medium	2.60
Fine	6.50

The computational meshes for the three grid levels are illustrated in Figure 10. The refinement ratio (r) between successive grids is maintained at 2.5, ensuring systematic mesh refinement.

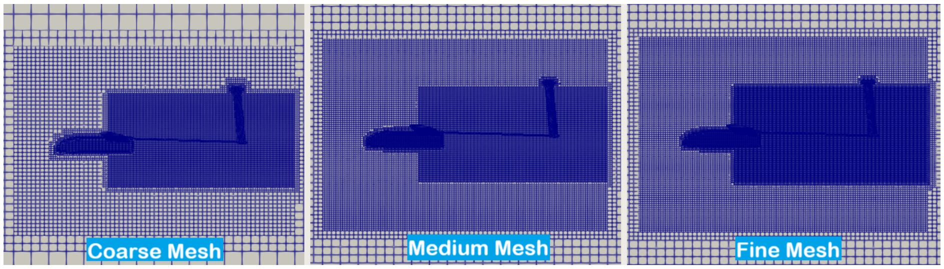

Figure 10: Cross-sectional view of the computational mesh for different mesh densities

To quantify the discretisation error and validate mesh independence, **Richardson Extrapolation** and the **Grid Convergence Index (GCI)** method were applied [8]. The lift coefficient (C_L) values for the coarse, medium, and fine meshes were obtained and reported in Table 6. Richardson Extrapolation was used to predict the solution as the grid spacing approaches zero, yielding an extrapolated C_L value of 0.5053. This value is closely aligned with the fine mesh result, reinforcing the consistency and reliability of the solution.

Table 6: C_L values and Grid Convergence Index (GCI) results for different mesh densities

Grid Level	C_L
Coarse	0.5154
Medium	0.5186
Fine	0.5106

The Grid Convergence Index (GCI), which quantifies the numerical uncertainty between grid levels, was calculated for both coarse-to-medium and medium-to-fine transitions. The GCI values were found to be 0.67% and 0.27%, respectively, below the 1% threshold, indicating strong mesh convergence and high confidence in the solution accuracy.

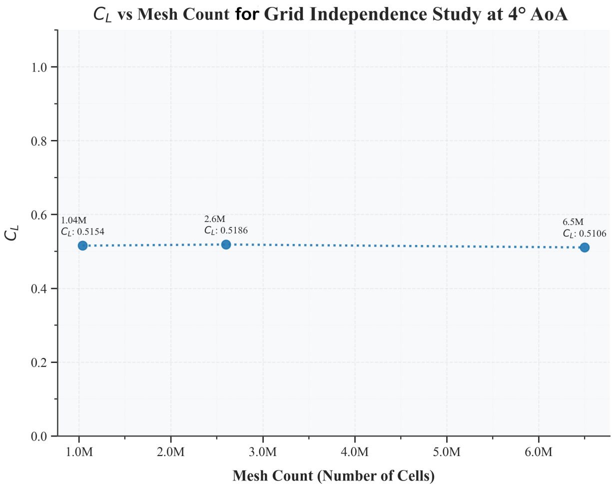

Figure 11: C_L values for different mesh densities

The results of the grid convergence study indicate that the solution is largely independent of mesh resolution for the medium and fine grids. Consequently, the medium mesh was selected for subsequent aerodynamic analyses as it optimally balances computational cost and numerical accuracy.

4.3 Baseline UAV Study

To benchmark our OpenFOAM implementation against the original Ansys Fluent results reported by Meftah et al., we reconstructed the baseline UAV geometry as far as possible given the incomplete geometric data. In particular, the key dimensions like exact length and cross-section of fuselage, chord length of tail and distance between wing and tail were not specified in the original paper and had to be estimated from published schematics and scaled drawings. These assumptions introduce a small but unavoidable source of discrepancy in the predicted aerodynamic coefficients.

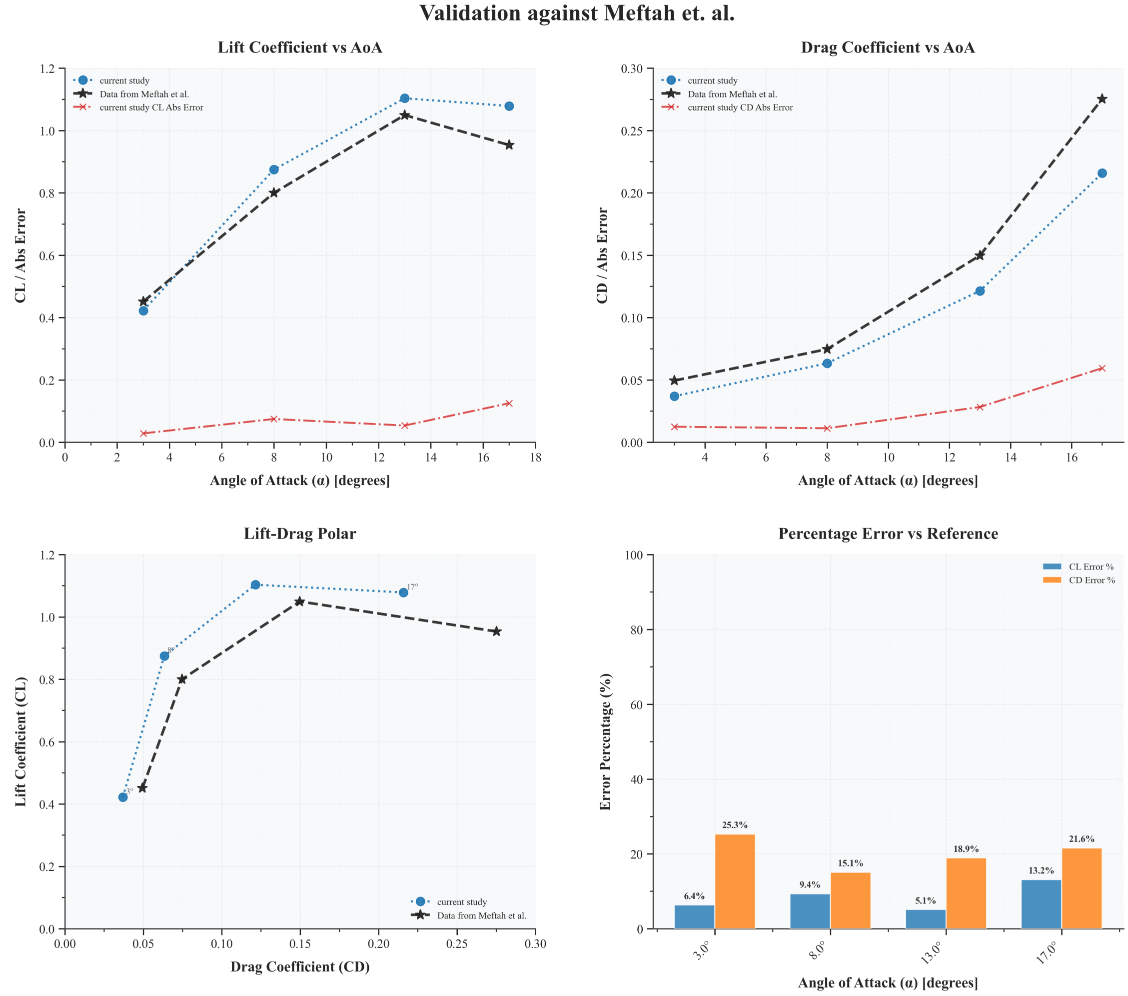

Figure 12: Comparison of lift and drag coefficients versus angle of attack (AoA) between the present OpenFOAM simulations and Meftah et al. Absolute errors in C_L and C_D are plotted in red.

Figure 12 shows that our OpenFOAM predictions of lift (C_L) and drag (C_D) closely match the reference data, capturing the linear lift region and the stall onset at 13°. The maximum absolute errors are 0.13 in C_L (≈13.2%) and 0.06 in C_D (≈21.6%) at 17°. In the 0° to 13° range, deviations remain below 0.08 in C_L (≤9.4%) and 0.03 in C_D (≤18.9%).

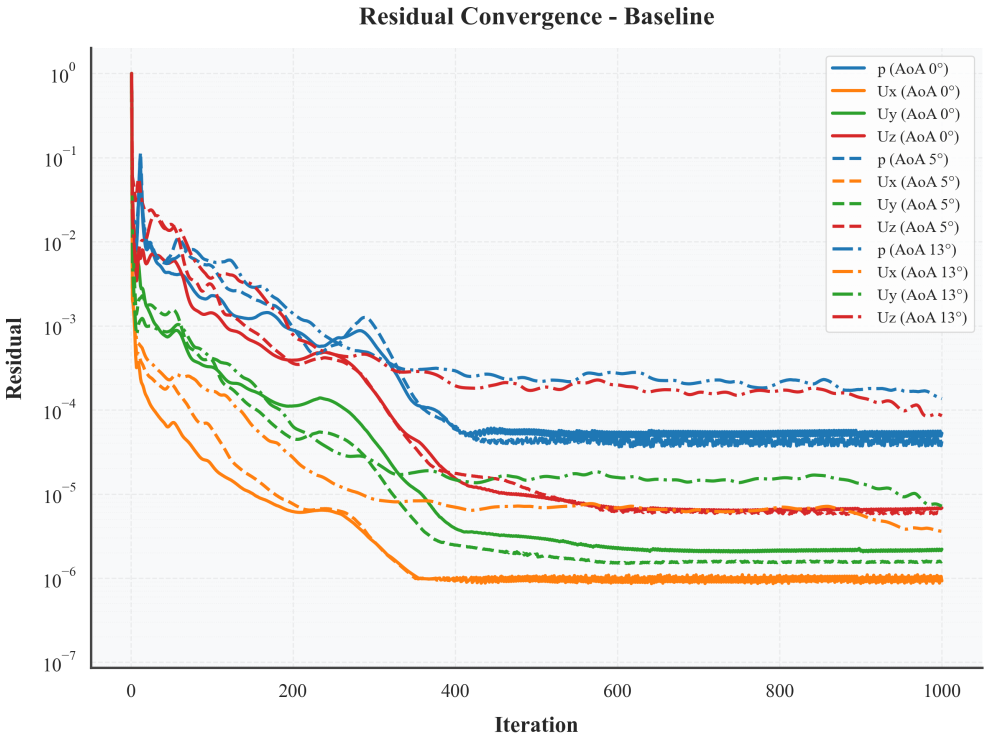

Figure 13: Residual convergence for pressure and velocity components at AoA = 0°, 5°, and 13° in the baseline OpenFOAM runs

As illustrated in Figure 13, continuity and momentum residuals at all AoA decrease by at least five orders of magnitude within 1,000 iterations. Final residuals reach approximately 10^{-6}–10^{-7} for velocity and 10^{-4}–10^{-5} for pressure, demonstrating stable and robust solver performance. The slight overprediction of lift and underprediction of drag at high AoA are likely due to our geometric estimations, particularly the fuselage wing junction and V-tail size and placement, which affect local separation patterns. With this baseline validation complete, we proceed to parametric geometry studies.

4.4 Winglet Cant Angle Study

The winglet cant angle study aims to understand the aerodynamic influence of the blended winglet at different cant angle configurations. Two winglet configurations were studied: a 90° winglet and a 45° winglet. The UAV wings were slightly extended to facilitate smooth blending with the winglets, resulting in a noticeable increment in the lift coefficient (C_L) compared to the baseline. However, this extension also introduced a slight increase in drag coefficient (C_D), which somewhat balanced the lift-to-drag ratio (C_L/C_D).

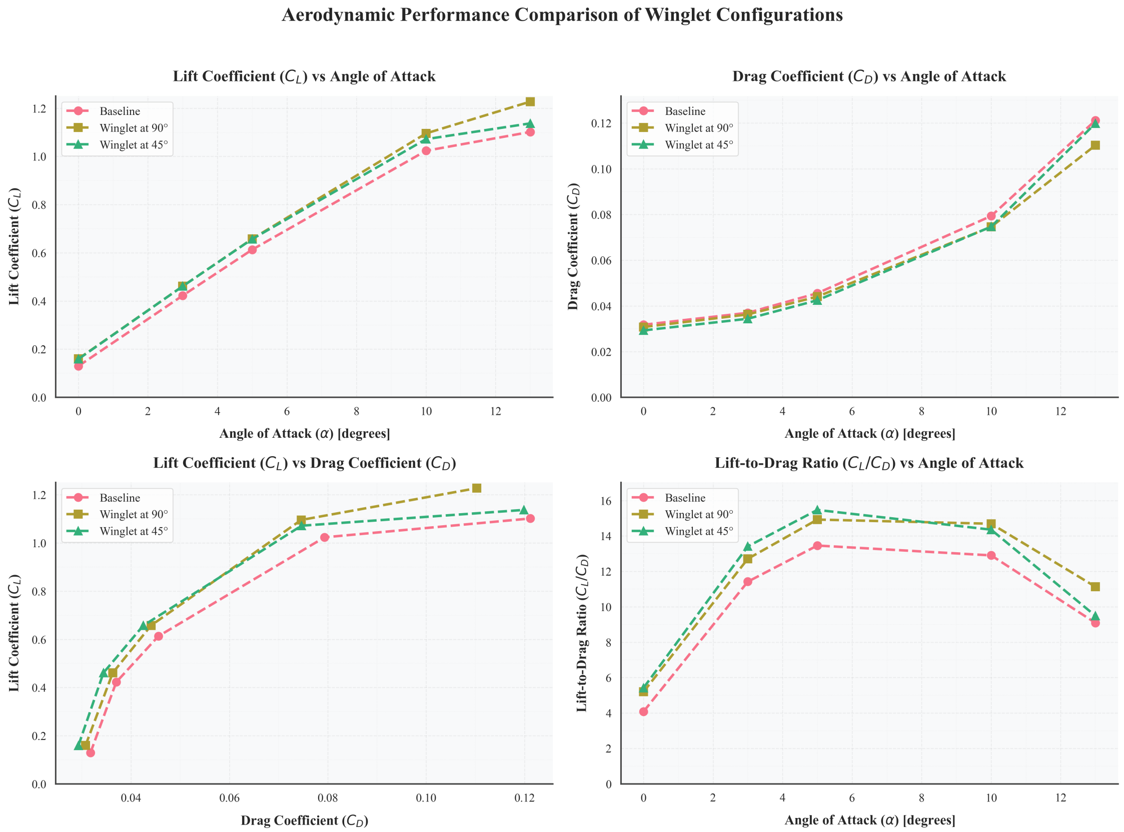

Figure 14: Aerodynamic Performance Comparison of Winglet Configurations

Lift Coefficient (C_L) vs. Angle of Attack (α): Both winglet configurations demonstrated higher C_L values across all angles of attack when compared to the baseline, with the 45° winglet showing the most improvement. The smoother transition near the stall region indicates enhanced lift generation due to improved wingtip vortex management. Drag Coefficient (C_D) vs. Angle of Attack (α): Although the introduction of winglets increased parasitic drag slightly, C_D of the UAV with winglets were lower than that of the baseline UAV. The 45° configuration maintained a lower C_D than the 90° configuration. This suggests that the angled design mitigates induced drag more effectively for this configuration. Lift Coefficient (C_L) vs. Drag Coefficient (C_D): The C_L vs. C_D curve shows a better aerodynamic efficiency for both winglets compared to the baseline. The 45° winglet outperforms the 90° one by maintaining higher C_L for the same C_D, indicating superior lift generation relative to drag due to an increase in effective wingspan. Lift-to-Drag Ratio (C_L/C_D) vs. Angle of Attack (α): The 45° winglet achieved the highest aerodynamic efficiency, with a maximum improvement of 14.95% over the baseline, whereas the 90° winglet, although effective, trailed slightly with a 10.9% improvement at $\alpha = 5°$. The results signify that the 45° cant angle is more optimal for drag reduction. Overall, it clearly illustrates the benefits of winglet optimisation for enhanced aerodynamic performance.

4.5 Flow Visualisation and Spanwise Flow

This section presents the flow visualisation analysis for the baseline UAV and winglet configurations. The visualisation includes pressure contours, velocity fields, and spanwise flow patterns to understand the aerodynamic characteristics and the impact of winglets on vortex strength and induced drag. Figures 15 and 16 illustrate the pressure distribution and velocity contours at the cross-section of the flow field for the baseline UAV across five different angles of attack $(0°, 3°, 5°, 10°, 13°)$. The pressure distribution clearly shows regions of high pressure near the leading edge and low pressure over the upper surface, generating lift. As the angle of attack increases, the low-pressure region intensifies, leading to an increase in lift before finally reducing due to flow separation in the post-stall region. The velocity contours demonstrate flow acceleration over the wing surfaces and deceleration near the trailing edges in the linear region.

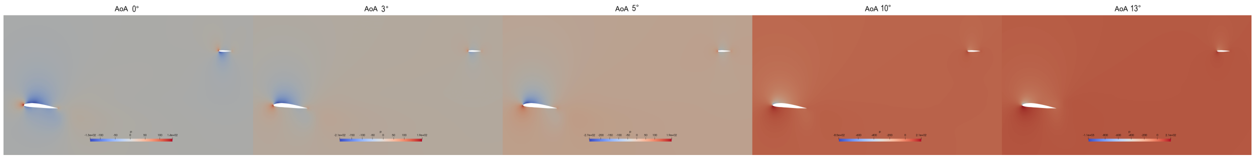

Figure 15: Pressure Distribution at Cross-Section for Baseline UAV at Various Angles of Attack

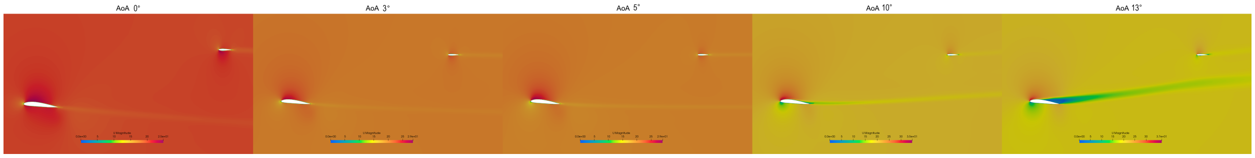

Figure 16: Velocity Contours at Cross-Section for Baseline UAV at Various Angles of Attack

The surface pressure distribution for the baseline UAV is shown in Figure 17. This visualisation helps identify high-pressure zones and low-pressure zones on the surfaces, which directly influence aerodynamic forces.

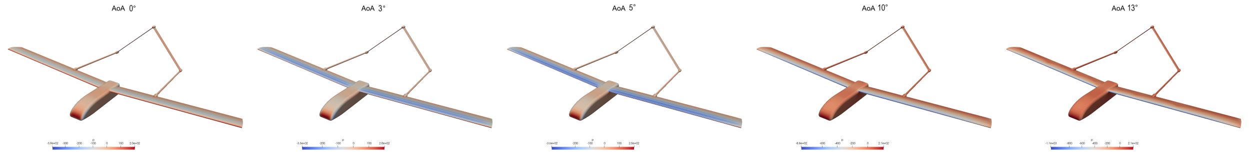

Figure 17: Surface Pressure Distribution for Baseline UAV at Various Angles of Attack

4.5.1 Spanwise Flow Analysis

Spanwise flow directly leads to wingtip vortex formation and thus causes induced drag. The visualisation of spanwise velocity at the trailing edge for the baseline UAV, winglet at 45°, and winglet at 90° is illustrated in Figures 18, 19, and 20, respectively.

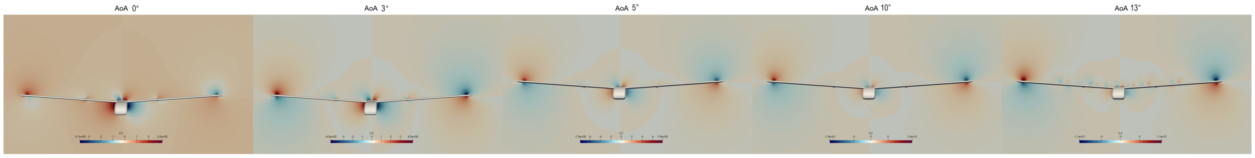

Figure 18: Spanwise Flow Visualisation at Trailing Edge for Baseline UAV at Various Angles of Attack

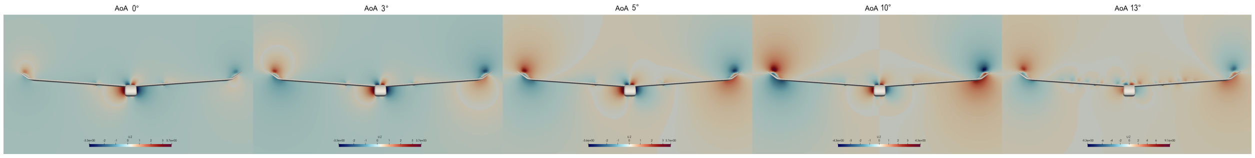

Figure 19: Spanwise Flow Visualization at Trailing Edge for Winglet at 45° at Various Angles of Attack

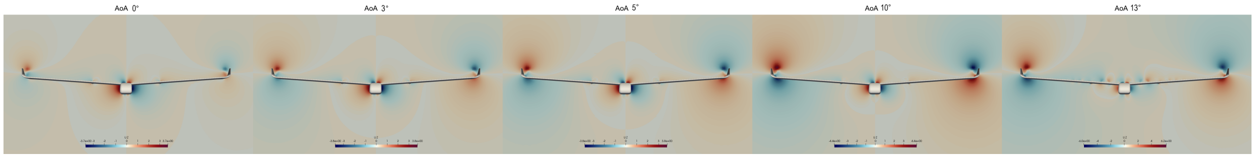

Figure 20: Spanwise Flow Visualization at Trailing Edge for Winglet at 90° at Various Angles of Attack

Spanwise flow originates from the pressure difference between the upper and lower wing surfaces. This, combined with the aircraft's forward motion, creates strong wingtip vortices that dissipate energy. Furthermore, the downwash created behind the wing reduces the effective angle of attack, which tilts back the lift vector, turning one of its components into drag called induced drag [9]. So, these vortices are a primary source of induced drag. The addition of winglets modifies this spanwise flow by acting as a physical barrier that reduces flow leakage from the lower wing surface to the upper wing surface around the wingtip [10]. This suppression minimises the strength of the wingtip vortices, as observed in Figures 19 and 20. The 45° winglet shows more effective reduction in spanwise flow compared to the 90° configuration, correlating with the improved (C_L/C_D) ratio observed in the performance analysis.

The wingtip vortices were visualised by using Q-criterion, which defines vortices as areas where the vorticity magnitude is greater than the magnitude of the rate of strain [11]. Figure 21 shows an iso-surface with Q = 2000 on the flow domain with velocity magnitude colouring for baseline UAV and UAV with winglet at 45° at 5° angle of attack. While the vorticial structures behind the wake region of the fuselage are largely unaffected, the wingtip vortices on the UAV with a winglet are reduced drastically, reinforcing the effectiveness of the winglet.

Thus, the winglets can enhance lift generation and contribute to drag reduction for the UAV by mitigating induced drag through reduction of wingtip vortices, confirming their aerodynamic advantage in UAV configurations.

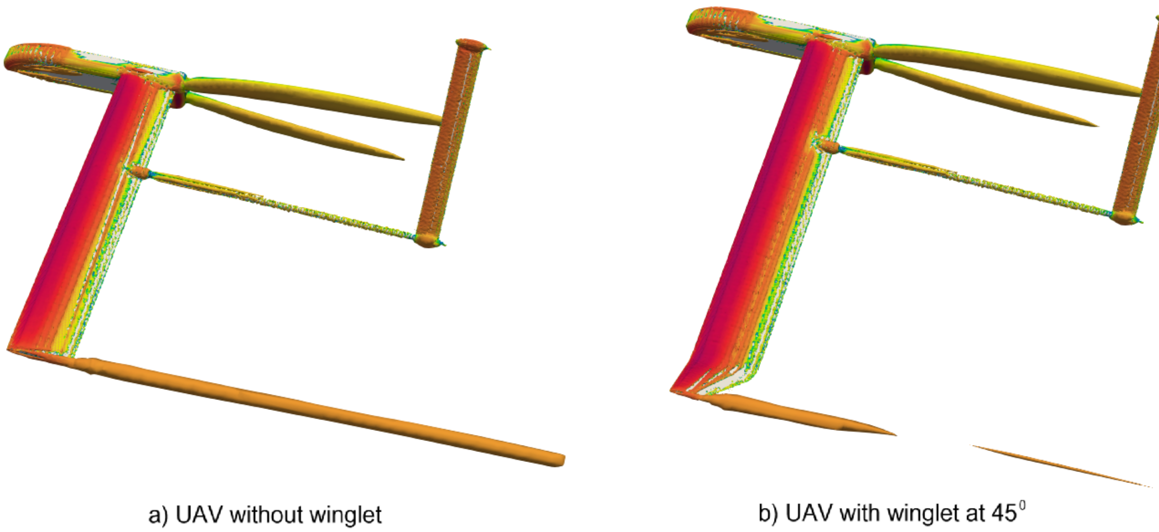

Figure 21: isosurfaces for Q=2000 for baseline UAV and UAV with winglet at 45° at 5° Angles of Attack. The colour on the isosurface represents the magnitude of velocity.

5 Limitations

The original study of Meftah et al. [3] makes the comparison between the numerical study of UAV with wing incidence of 4° and experimental study of isolated wing and plots C_z vs incidence and C_x vs incidence. It was assumed C_x and C_z are C_D and C_L. Also, the study doesn't provide complete data about geometry and appropriate assumptions based on proportions observed in the figure were made for any missing geometry data. These are the assumptions made when trying to interpret and translate the original work. The current study has an average y+ value of 18, which might not well resolve the boundary layer, accounting for some errors in the study. Also, steady state assumptions made may not well resolve vortices and other truly unsteady flow behaviour. As the current study focuses on aerodynamic performance and the effect of winglets rather than vortex structures influencing them, less emphasis was put on an in-depth study of the vortices formed.

6 Conclusion

The aerodynamic analysis of the fixed-wing UAV with inverted V-tail configuration, extended with winglet integration, provides key insights into the impact of winglet cant angles on aerodynamic efficiency. The CFD simulations were carried out for three configurations: the baseline configuration without a winglet, a UAV with a winglet at 90°, and a UAV with winglet at 45°. The results demonstrate clear improvements in the aerodynamic performance of the UAV with the addition of winglets. The C_L and C_D vs. α plots indicate that both winglet configurations enhance the lift characteristics and reduce drag compared to the baseline. This improvement is caused by the reduction in spanwise flow leakage, which mitigates induced angle of attack, thus slightly increasing lift and reducing induced drag. The 45° winglet showed the highest lift generation among the three configurations. C_L/C_D experienced a maximum improvement of 10.9% for the 90° winglet and 14.95% for the 45° winglet. This confirms that the aerodynamic benefits from induced drag reduction and vortex mitigation outweigh the additional parasitic drag penalty introduced by the winglets. The findings indicate that strategic winglet design, particularly cant angle optimisation, can significantly enhance UAV aerodynamic efficiency by controlling spanwise flow and mitigating induced drag. For future work, the design optimisation of winglets across various parameters might yield further improvements. Ultimately, this study demonstrates the practical benefits of winglets in UAV design, offering enhanced range, endurance, and operational efficiency in real-world applications in low Reynolds number flight.

7 Future Recommendations

The study was limited to the analysis of steady behaviour, primarily due to the limitations of the internship's time. For future work, the study should be expanded to account for the unsteady nature of the flow. This could involve running transient simulations with changing angles of attack to understand how these variations affect the local flow field over time. Although this study focused heavily on overall aerodynamic performance, it largely overlooked vortices and their specific effect. Conducting a more dedicated, vortex-focused study would be very beneficial [12]. The action of control surfaces, particularly the elevator, is crucial for changing the angle of attack in real flight, and this was completely ignored here. A more thorough study is certainly needed to assess its effect. Furthermore, while this work covered cruise and steady flight, studying general turning flight is equally important for understanding the UAV's performance in a true sense and should be the focus of a subsequent study. This research can also be further expanded by investigating the effect of various types of winglets on improving flight performance and potentially generating a surrogate model [13] or with CFD-based optimization [14] to optimize the design of a winglet for this specific UAV.

Acknowledgement

This work was supported by the FOSSEE project under the National Mission on Education through ICT, Ministry of Education, Government of India. The author acknowledges the mentorship provided by FOSSEE mentor Manjil Sitoula and the guidance provided by the supervisors Prof. Chandan Bose, Prof. Tushar Chourushi and CFD Engineer Mr. Nikhil Bhamare. The author also extends gratitude to Mrs. Payel Mukherjee, Project Manager, CFD-Openfoam Team, FOSSEE, for her continuous support during the internship period. This work couldn't have been completed without access to the workstation from IIT Bombay FOSSEE, for which the author is very grateful.

References

[1] H. Shakhatreh, A. H. Sawalmeh, A. Al-Fuqaha, Z. Dou, E. Almaita, I. Khalil, N. S. Othman, A. Khreishah, and M. Guizani, ‘‘Unmanned aerial vehicles (uavs): A survey on civil applications and key research challenges,’’ *IEEE Access*, vol. 7, pp. 48 572–48 634, 2019.

[2] M. Nasir, M. Z. Yusoff, and N. M. Ariff, ‘‘A review of winglets on tip vortex, drag and airfoil geometry,’’ *Journal of Advanced Research in Fluid Mechanics and Thermal Sciences*, vol. 72, no. 2, pp. 79–90, 2020.

[3] S. M. A. Meftah, B. Imine, O. Imine, and L. Adjlout, ‘‘Numerical simulation of a flow around an unmanned aerial vehicle,’’ *Mechanika*, vol. 17, no. 2, pp. 193–196, 2011.

[4] J. H. Ferziger and M. Perić, *Computational Methods for Fluid Dynamics*, 4th ed. Springer International Publishing, 2020.

[5] P. R. Spalart and S. R. Allmaras, ‘‘A one-equation turbulence model for aerodynamic flows,’’ American Institute of Aeronautics and Astronautics, Tech. Rep. AIAA Paper 92-0439, 1992, presented at the 30th Aerospace Sciences Meeting & Exhibit, Reno, NV.

[6] D. Greenblatt and D. R. Williams, ‘‘Flow control for unmanned air vehicles,’’ *Annual Review of Fluid Mechanics*, vol. 54, no. Volume 54, 2022, pp. 383–412, 2022.

[7] J. Anderson, John D., *Fundamentals of Aerodynamics*, 6th ed. McGraw-Hill Education, 2017.

[8] P. J. Roache, ‘‘Quantification of uncertainty in computational fluid dynamics,’’ University of Limerick, Tech. Rep., 1997.

[9] J. Anderson, John D., *Introduction to Flight*, 9th ed. McGraw-Hill Education, 2019.

[10] J. Jupp, ‘‘Wing aerodynamics and the science of compromise,’’ *Aeronautical Journal*, vol. 105, pp. 633–641, 2001.

[11] J. JEong and F. Hussain, ‘‘On the identification of a vortex,’’ *Journal of Fluid Mechanics*, vol. 285, pp. 69–94, 1995.

[12] J. C. Chan, H. Hesse, and P. C. Wang, ‘‘Les validation on near-field wingtip vortex evolution with wind tunnel characterization at low reynolds number,’’ *Aerospace Science and Technology*, vol. 157, 2 2025.

[13] E. Nikolaou, S. Kilimtzidis, and V. Kostopoulos, ‘‘Winglet design for aerodynamic and performance optimization of uavs via surrogate modeling,’’ *Aerospace*, vol. 12, 1 2025.

[14] P. Panagiotou, P. Kaparos, and K. Yakinthos, ‘‘Winglet design and optimization for a male uav using cfd,’’ *Aerospace Science and Technology*, vol. 39, pp. 190–205, 2014.

DISCLAIMER